Freie Universität Berlin

Title:

Hydrophobicity of Self-Assembled Monolayers of Alkanes: Fluorination, Density, Roughness, and Lennard-Jones Cutoffs

＋

Author(s): Shane Carlson, Maximilian Becker, Florian N. Brünig, Kenichi Ataka, Rubén Cruz, Leixiao Yu, Peng Tang, Matej Kanduč, Rainer Haag, Joachim Heberle, Hesam Makki, and Roland R. Netz

Document type: Postprint

Hydrophobicity of Self-Assembled Monolayers of Alkanes: Fluorination, Density, Roughness, and Force Cutoffs

Shane Carlson[1], Maximilian Becker[1], Florian N. Brünig[1], Kenichi Ataka[1], Rubén Cruz[1], Leixiao Yu[2], Peng Tang[2], Hesam Makki[3], Matej Kanduč[4], Rainer Haag[2], Joachim Heberle[1], and Roland R. Netz[1]

[1]Fachbereich Physik, Freie Universität Berlin, Arnimallee 14, 14195 Berlin, Germany
[3]Polymer and Color Engineering, Amirkabir University of Technology, 424 Hafez Ave, Tehran, Iran, 15875-4413
[4]Institut für Chemie und Biochemie, Freie Universität Berlin, 14195, Berlin, Germany
[4]Department of Theoretical Physics, Jožef Stefan Institute, Jamova cesta 39, 1000 Ljubljana, Slovenija

August 4, 2021

Abstract

The interplay of fluorination and structure of alkane self-assembled monolayers and how these affect hydrophobicity is explored via molecular dynamics simulations, contact angle goniometry, and SEIRA spectroscopy. Wetting coefficients are found to grow linearly in monolayer density for both alkane and perfluoroalkane monolayers. The larger contact angles of monolayers of perfluorinated alkanes are shown to be primarily caused by their larger size, which leads to a larger nearest-neighbor grafting distance and smaller tilt angle. Increasing the dispersion force cutoff in simulations is found to increase hydrophilicity. Specifically, wetting coefficients scale like the inverse square of the cutoff, and when extrapolated to the infinite cutoff limit, yield contact angles that compare favorably to experimental values. Nanoscale roughness is also found to reliably increase monolayer hydrophobicity, mostly via the reduction of the entropic part of the work of adhesion. Analysis of depletion lengths show that droplets on nanorough surfaces penetrate into the surface partially, intermediate between Wenzel and Cassie-Baxter states.

Introduction

Fluorination has long been a primary strategy in the synthesis of hydrophobic (as well as oleophobic) compounds, surfaces, and coatings. Examples include hydrophobic diamond-like carbon surfaces [1], amphiphobic latex films [2], non-biofouling surfaces [3] and nanoparticles [4], self-cleaning sol-gels [5] and fabrics [6], and water-oil separating glass fiber mats [7]. This hydrophobicity, coupled with the relatively small size and chemical inertness of fluorine, has fostered interest in the substitution of fluorine into organic compounds in medicinal chemistry [8]. These have biochemical implications for enzyme substrate recognition, the hydrolytic stabilization of orally ingested compounds, and drug metabolism and transport: for example, the hydrophobicity of fluorinated compounds has been credited with easing their crossing of the blood-brain barrier [8]. Hydrophobicity of surfaces has a significant impact on protein adsorption [9] and on the behavior of the adsorbed proteins [10].

Self-assembled monolayers (SAMs) of alkanethiols ($SH(CH_2)_nCH_3$) on gold, whose head (ligand) and tail (terminal) groups can be easily tailored, make excellent model systems for understanding self-organization, interfacial phenomena, and structure-behavior relationships [11, 12]. Preparation of partially-fluorinated or perfluorinated aliphatic SAMs ($SH(CH_2)_n(CF_2)_mCF_3$) is similarly facile, and with these also being more thermally stable, better antibiofouling agents, more chemically and biologically inert, and more oleo- and hydrophobic, they have also gained prominence as a model system for fluorinated thin films and seen application in various technologies [13]. Fluorinated SAMs (F-SAMs), with three or more fluorinated carbons at the tail, have been shown to have larger contact angles (more oleo-/hydrophobic) with various liquids than their aliphatic counterparts (H-SAMs) [14, 15].

In this work, we use classical molecular dynamics (MD) simulations to study the interplay among SAM fluorination, the packing density of the SAM ligand adlayer on the substrate, the SAM tilt angle, SAM roughness, and Lennard-Jones cutoff distance, and how these in turn influence hydrophobicity. We find that the chain grafting density and tilt angle of a SAM influence contact angles by changing the atomic number density of the SAM, with a very similar linear relationship between wetting coefficients and carbon number density for H-SAMs and F-SAMs. The tilt angle of our simulated F-SAM

also agrees well with our experimental result for the same system obtained via surface enhanced infrared absorption spectroscopy (SEIRAS). Further, extrapolating contact angles to the infinite Lennard-Jones cutoff distance, or using a Lennard-Jones particle mesh Ewald (LJ PME) scheme [16, 17], which accounts for long-range interactions, gives contact angles that agree well with experimental values. Finally, we find that nanoroughness tends to increase hydrophobicity mostly via a roughness-induced decrease in adhesion entropy, with water penetrating partially into nanoroughened SAMs.

[kJ/mol]	$C_H C_F C_F C_F$	$C_H C_H C_F C_F$	$C_H C_H C_H C_F$
C_0	5.8483	1.0883	-1.6214
C_1	-9.6567	-2.8142	0.4758
C_2	-6.5034	-2.1359	-2.3283
C_3	2.7175	3.5452	0.1497
C_4	7.0042	3.0998	3.5359

Table 1: Ryckaert-Bellemans (eq (1)) coefficients in kJ/mol for dihedral angles found by optimization, as shown in Figure 1a. Dihedrals C_H-C_F-C_F-C_F and C_H-C_H-C_F-C_F are optimized in an H2F6 molecule, while C_H-C_H-C_H-C_F is optimized in H7F1. The coefficient C_5 is zero for all three dihedrals.

Methods

Force Field MD Simulation Details

Force field MD simulations are carried out in single-precision GROMACS 2019.6 [18, 19], using the leap-frog integrator with a time step of 2 fs [20]. Boundaries are periodic in all directions. Simulations are in the NVT ensemble, using the velocity-rescaling (CSVR) thermostat at 300 K [21]. SAM molecules are modeled using the OPLS All-Atom (OPLS-AA) force field with selected dihedrals optimized by us (see below) [22, 23, 24]. Water is modeled using the SPC/E water model [25]. Unless otherwise noted, the Lennard-Jones force cutoff is set to 1 nm. The force-switching scheme is used and the switch distance is always set to 0.1 nm shorter than the cutoff. Equilibrium trajectories are 60 ns in total, and are split into ten 6-ns subtrajectories in the analysis in order to estimate variances where possible. SAMs are restrained by a harmonic potential applied to the bottom carbon of each molecule with spring constant $k = 25000$ kJ/(mol nm^2), unless otherwise noted. We simulate "H-SAMs" comprising decane, $CH_3(CH_2)_8CH_3$, or "H10" molecules, and "F-SAMs" comprising $CH_3CH_2(CF_2)_7CF_3$ or "H2F8" molecules. The nearest neighbor distance between restraint positions is 4.97 Å for H-SAMs and 5.90 Å for F-SAMs, unless otherwise noted.

Dihedral Optimization

We employ the OPLS All-Atom (OPLS-AA) force field for which, following a procedure outlined in Ref. [26], we optimize three dihedral angle potentials. This is done because fluorinated and hydrogenated carbon chains have significantly different dihedral energy profiles, and literature values are not available for backbone dihedrals that cross between them. The optimized dihedrals are highlighted in the schematics in Figure 1a. Potential energy scans are taken over the dihedral angles in vacuum using ab initio calculations (MP2/cc-pVTZ//HF/6-31G*), with the molecular geometry first energy-minimized at that angle. The same scans are taken using the OPLS-AA force field, with the relevant dihedral energy set to zero. The difference between these is then fit with the Ryckaert-Bellemans potential

$$V_{\text{dih}}(\psi) = \sum_{n=0}^{5} C_n \cos^n(\psi - 180°), \qquad (1)$$

where ψ is the dihedral angle and C_n are coefficients adjusted in the fit. Figure 1a shows the resulting fitted dihedral potentials, the vacuum ground state molecular potential energies in OPLS-AA with the new dihedral potentials included, and the original targeted ab initio potential energies. For all three dihedrals, the newly optimized OPLS-AA force field approximates the energy profile of the ab initio model very well. The resulting optimized coefficients for eq (1) are reported in Table 1.

Comparing Water Structure Against DFT MD

The OPLS-AA force field employed was tested by simulating solvated single molecules of hexane with one fluorinated terminal group, $CH_3(CH_2)_4CF_3$ (see the schematic in Figure 1b), in water at 300 K, and comparing to the results for the same system simulated using density functional theory (DFT) MD. The DFT MD simulations consist of ten 15-ps NVE trajectories (initial conditions from an equilibrium NVT trajectory at 300 K) of a single molecule in 128 waters, carried out in CP2K
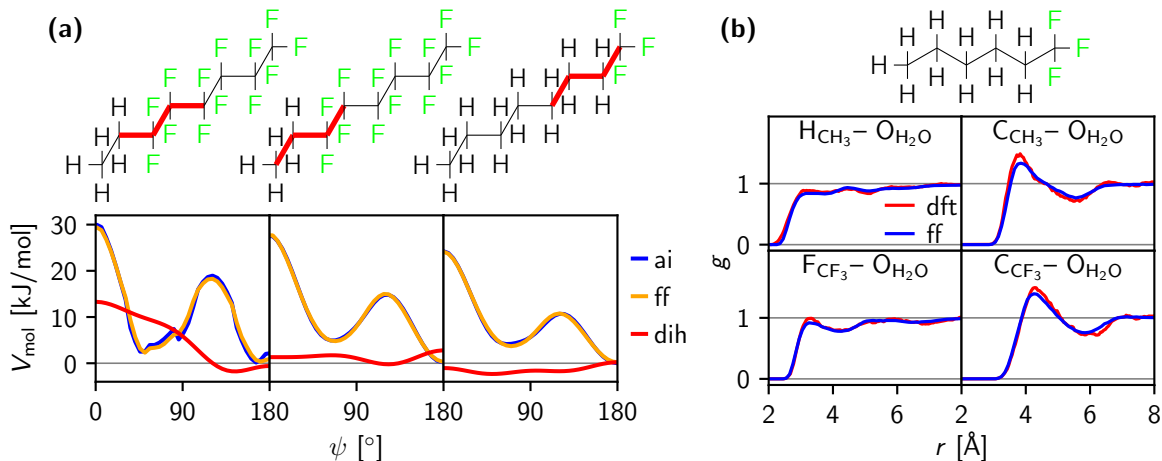
Figure 1: **(a)** Ground state vacuum molecular potential energies over backbone dihedral angles from ab initio calculations and our own optimized OPLS-AA force field, along with the fitted Ryckaert-Bellemans potentials (eq (1)). The dihedrals are indicated in the schematics above the plots. The fit parameters from the optimization are reported in Table 1. **(b)** Radial density distributions of water oxygens relative to atoms of the CH_3 (top panels) and CF_3 (bottom panels) headgroups of single solvated hexane molecules with a single fluorinated headgroup (see schematic) from DFT and force field MD simulations at 300 K. The left panels show profiles relative to the H and F atoms, the right panels, profiles relative to the respective terminal carbons.

6.1 [27] using the BLYP exchange-correlation functional [28] with Grimme-D3 dispersion correction [29] and DZVP-MOLOPT-SR-GTH basis set [30], a 0.5-fs time step, and 400-Ry plane-wave cutoff. Figure 1b shows comparisons of radial distributions of water oxygen relative to H and C atoms in the terminal CH_3 group (top row), and relative to F and C atoms in the terminal CF_3 group (bottom row) from both models. The two models agree remarkably well for all four distributions, with slight overstructuring of the water in the first hydration shell for the DFT MD data compared to the force-field MD data, which may be related to a known inaccuracy of BLYP for water [31]. This indicates excellent modeling of water structure near CH_3 and CF_3 groups by the OPLS-AA force field used.

Contact Angle Goniometry

Water contact angles are measured experimentally on H-SAMs ($SH(CH_2)_9CH_3$ on Au(111)) and F-SAMs ($SH(CH_2)_2(CF_2)_7CF_3$ on Au(111)). These are the same systems as those simulated, with the S–C bonds modeled *in silico* via a harmonic restraint potential applied to the carbon. Measurements are carried out using a DataPhysics Instruments goniometer at room temperature. Fifteen measurements are taken from each of five samples. Static contact angles are measured on sessile 2-μm

Milli-Q water droplets equilibrated for 15 s. Advancing (receding) contact angles are found by leaving the needle in the droplet, adding (removing) water at 0.1 μL/s, and recording the contact angle once the contact line at the base of the droplet has begun to move [32].

SAM Tilt Angle via SEIRAS

The tilt angle of an F-SAM ($SH(CH_2)_2(CF_2)_7CF_3$ on gold) was also determined from surface enhanced infrared absorption spectroscopy (SEIRAS). The SEIRAS spectrum of the SAM is compared to the attenuated total reflection (ATR) FTIR spectrum of liquid $SH(CH_2)_2(CF_2)_7CF_3$. The intensities of bands at approximately 1330 and 1146 cm^{-1} are extracted via fitting and the tilt angle is obtained from their ratio.

Results and Discussion

Water Contact Angle from Simulation

We extract "microscopic" water contact angles θ_μ from MD simulations of cylindrical droplets on H-SAMs and F-SAMs (see Figure 2a) [33]. Cylin-
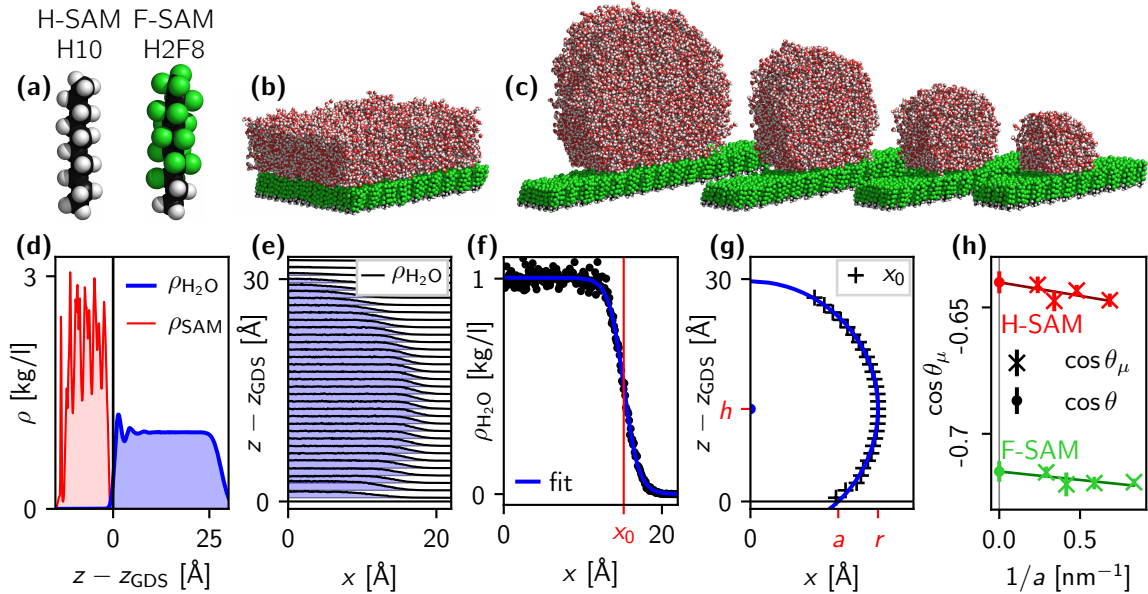
3

Figure 2: Workflow for extracting contact angles from MD simulations. **(a)** H10 and H2F8 molecules, which constitute simulated H-SAMs and F-SAMs respectively. **(b)** Simulation snapshot of a planar water slab on an F-SAM. **(c)** Snapshots of the four different sizes of cylindrical droplets simulated (8192, 4096, 2048, and 1024 water molecules) shown here on F-SAMs. **(d)** Density histograms along z of a water slab and SAM (as in (b)), used to locate the Gibbs dividing surface at the base of the water slab, z_{GDS}. **(e)** Density histograms along x of slices of the 1024-molecule water droplet (as shown on the right in (c)) at different heights z, plotted together schematically. **(f)** The density profile from (e) for height $z - z_{\mathrm{GDS}} \in [20, 21]$ Å (data points), along with a fit of the sigmoid function eq (3) (solid line), for extracting the droplet surface position x_0. This is done for each profile. **(g)** The resulting surface data $x_0(z)$ from the sigmoidal fits, like the one in (f), along with the corresponding circle fit (solid line), which gives the droplet radius r, droplet footprint radius a, and height h (and therefore also the microscopic contact angle θ_μ). **(h)** Cosine of microscopic contact angle θ_μ plotted over $1/a$ for the four droplet sizes shown in (c) on an H-SAM and an F-SAM (see (a)). Also shown are linear fits, used to extrapolate to $1/a = 0$ to obtain the macroscopic contact angle θ according to the modified Young's equation, eq (4).

drical droplets greatly reduce the finite-size effects introduced by the line tension at the SAM-water-vapor triphasic boundary [34]. Extracting θ_μ from several differently sized systems allows us to extrapolate to the contact angle θ in the macroscopic limit, following a method employed in Refs. [34, 35, 36].

To measure the contact angle from a microscopic droplet simulation, the following procedure is followed (see also Figures 2d-g):

Step 1 – Locate SAM/water interface: A 3-nm thick water slab is separately simulated on the SAM of interest, as shown in Figure 2b. The position of the Gibbs dividing surface of the water slab z_{GDS} is taken to define the position of the SAM/water interface for that system. The Gibbs dividing surface position is found via

$$z_{\mathrm{GDS}} = z_0 + \int_{z_0}^{z_l} \mathrm{d}z \left(1 - \frac{\rho_l(z)}{\rho_l^b} \right), \qquad (2)$$

where $\rho_l(z)$ is the water density profile along z, z_0 is a position well outside of the water slab where water density is zero, z_l is a position well inside the bulk of the water slab, and ρ_l^b is the bulk density of the water (see Figure 2d) [37].

Step 2 – Extraction of droplet density profiles: Cylindrical droplets, as illustrated in Figure 2c, are simulated on the SAM of interest. The simulation box above the SAM/water interface is divided into bins along z. At each timestep, the center of mass of the droplet is found and its x-position is set to zero (the cylindrical axis of the droplet is oriented along the y-direction). For each bin along z, the mass density along x of the droplet is recorded in a separate histogram. Over many timeframes, this builds an average density profile for each bin, as illustrated in Figure 2e.

Step 3 – Sigmoid fits for droplet surface: Each den-

4

sity profile is fit with a sigmoid function

$$\rho(x) = \frac{\rho_0}{2}\left(1 - \tanh\frac{x - x_0}{d}\right), \qquad (3)$$

where d gives the sharpness of the sigmoidal decay, and x_0 the position, as illustrated in Figure 2f. The droplet surface is then taken to be parametrized by $x_0(z)$.

Step 4 – Circle fit: A circle is fit to the $x_0(z)$ data, as shown in Figure 2g, which gives the microscopic contact angle θ_μ and droplet footprint radius a, defined at the Gibbs dividing surface z_{GDS}.

The macroscopic contact angle θ is related to θ_μ by the modified Young's Equation, which is derived in the SI Section S1, and reads

$$\cos\theta_\mu = \cos\theta - \frac{\tau}{\gamma_{lv}a}, \qquad (4)$$

where τ is the triphasic line tension, and γ_{lv} is the liquid-vapor surface tension [38]. This gives the scaling behavior of θ_μ in a, and can be used to extrapolate to $1/a = 0$, which gives θ. Note that this assumes that all finite-size effects in θ_μ scale in the same manner as the line tension τ [34].

Figure 2h shows two such extrapolations, one for an H-SAM and one for an F-SAM. For each SAM type, the contact angle is extrapolated from cylindrical droplet simulations of 1024, 2048, 4096, and 8192 water molecules, as illustrated in Figure 2c. It is clear here already that the simulated F-SAM is significantly more hydrophobic than its H-SAM counterpart, which is explored in detail below.

Dispersion Force Cutoff

The Lennard-Jones cutoff has been shown to be of particular importance in interfacial simulations in general [40, 41, 42]. Lennard-Jones forces are truncated at a distance R, typically about 1 nm, in order to save computational cost, and also to avoid interactions of a particle with more than one image of another particle over periodic boundaries. The introduction of a finite cutoff tends to have a more pronounced effect for interfacial properties than for bulk properties. Consider the potential energy for a monoatomic bulk condensed system,

$$E_{\text{pot}} = \int d\mathbf{r}\, g(r)V(r), \qquad (5)$$

where $V(r) = -r^{-6}$, i.e. only the long-range, attractive part of the Lennard-Jones potential is consid-

ered, and $g(r)$ is the distance-dependent pair correlation function, which is assumed to be constant for $r \geq R$. In spherical polar coordinates,

$$E_{\text{pot}} \propto \int_0^R dr\, 4\pi r^2 \frac{g(r)}{r^6} \qquad (6)$$

$$\propto \int_0^\infty dr\, \frac{g(r)}{r^4} - g(\infty)\int_R^\infty \frac{dr}{r^4}, \qquad (7)$$

which gives the result

$$E_{\text{pot}} = E_{\text{pot}}^0 + \Delta E_{\text{pot}}(R), \quad \Delta E_{\text{pot}}(R) \propto R^{-3}. \quad (8)$$

Figure 3a shows the dispersive potential energy from water-water interactions, $V_{\text{H}_2\text{O}}$, in a 3 nm-thick water slab, as a function of R^{-3}. The data appear linear as predicted by eq (8). Note that between $R = 1$ nm and $R \to \infty$, $V_{\text{H}_2\text{O}}$ changes by only roughly 2%, which is negligable.

The pressure can be found via the virial route

$$p = \frac{2}{3V}\left(E_{\text{kin}} - \xi\right), \qquad (9)$$

where V is the system volume and ξ is the trace over the virial tensor,

$$\xi = -\frac{1}{2}\int d\mathbf{r}\, g(r)rF(r), \qquad (10)$$

where $F(r) = -\frac{\partial}{\partial r}V(r) = -6r^{-7}$. The same procedure as for the energy above can be applied here, giving for the pressure

$$p = p_0 + \Delta p(R), \qquad \Delta p(R) \propto R^{-3}. \qquad (11)$$

Figure 3b shows the bulk mass density of a water slab, $\rho_{\text{H}_2\text{O}}$, as a function of R^{-3}. The density should be expected to be linear in the pressure, and therefore scale like R^{-3}, as given by eq (11), and indeed, the data are rather linear on this scale. Between $R = 1$ nm and $R \to \infty$, $\rho_{\text{H}_2\text{O}}$ changes by roughly 1%, which is also negligable.

On the other hand, consider $\varepsilon_{\text{int}}^{\text{LJ}}$, the areal dispersive interaction energy between a flat solid and an adsorbed liquid, separated by an interface and a depletion layer of thickness δ, again for the potential $V(r) = -r^{-6}$. This calculation is carried out in the SI Section S3, and gives

$$\varepsilon_{\text{int}}^{\text{LJ}} \propto \frac{1}{\delta^2} - \frac{6}{R^2} + \frac{8\delta}{R^3} - \frac{3\delta^2}{R^4}. \qquad (12)$$

Thus $\Delta\varepsilon_{\text{int}}^{\text{LJ}}(R) \propto R^{-2}$ to leading order, and since $\delta \ll R$, this is the predominant scaling behavior. Figure 3c shows $\varepsilon_{\text{int}}^{\text{LJ}}$ for water on H-SAMs and F-SAMs, extracted by summing pairwise dispersion
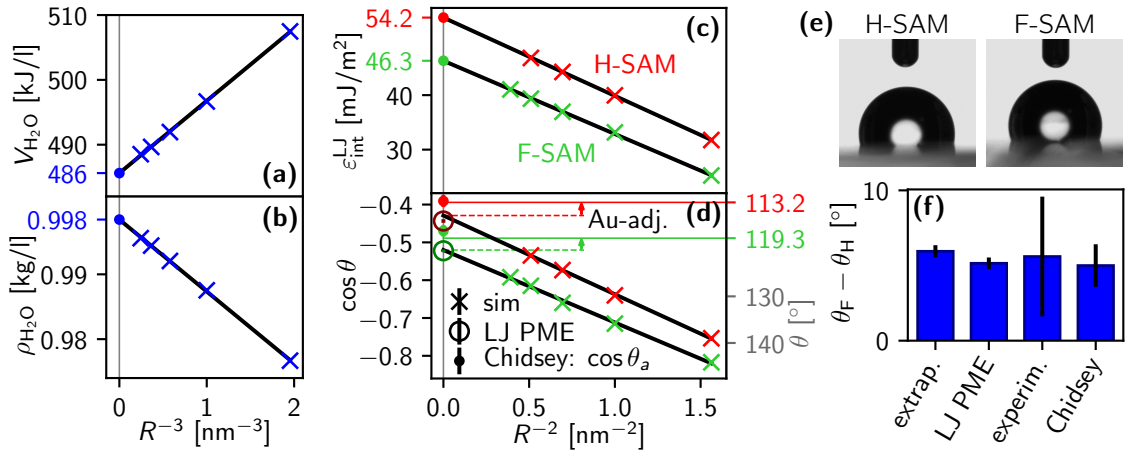
Figure 3: **(a-d)** Plots to demonstrate scaling behavior in the Lennard-Jones cutoff distance R, with extrapolations to the $R \to \infty$ limit. **(a)** Lennard-Jones potential energy due to intermolecular water-water interactions from water slab simulations, as a function of R^{-3}. **(b)** Bulk mass density of water slabs as a function of R^{-3}. **(c)** Areal dispersive SAM-water interaction energy as a function of R^{-2}, extracted from simulations of water slabs on H-SAMs and F-SAMs. **(d)** Cosine of simulated droplet contact angles on H-SAMs and F-SAMs as a function of R^{-2}. The extrapolated values at $R^{-2} = 0$ (dashed horizontal lines) compare favorably to those from LJ PME simulations. The extrapolated values are adjusted to account for the absent gold substrate (solid horizontal lines), and these agree well with experimental advancing contact angles from Ref. [39] (Chidsey), also shown. **(e)** Photos of droplets on H-SAMs and F-SAMs in the goniometer used in the experimental measurements. **(f)** The difference between F-SAM and H-SAM water contact angles. Included are data from the $R \to \infty$ extrapolations, those from LJ PME simulations, our own experimental advancing contact angles, and experimental advancing contact angles from Ref. [39] (Chidsey).

interactions from SAM-water slab simulations, as a function of R^{-2}. Note that, in this work, the sign of interaction energies such as $\varepsilon_{\text{int}}^{\text{LJ}}$ is chosen such that it is positive for an attractive surface. The data are rather linear for both SAM types, and unlike for the water potential energy and density discussed above, $\varepsilon_{\text{int}}^{\text{LJ}}$ changes by roughly 40% between $R = 1$ nm and $R \to \infty$ for F-SAMs.

The wetting coefficient $k = \cos\theta$ for a liquid-solid interface is linear in the work of adhesion, which is shown in the SI Section S4 to scale like the areal liquid-solid interaction energy ε_{int} for varying R. For an uncharged surface, ε_{int} is dominated by the dispersive contribution $\varepsilon_{\text{int}}^{\text{LJ}}$, so

$$k = k_0 + \Delta k(R), \qquad \Delta k(R) \propto R^{-2}. \tag{13}$$

Figure 3d shows $k = \cos\theta$ for H-SAMs and F-SAMs, extracted via the droplet-extrapolation technique, as a function of R^{-2}. These data are also linear, consistent with the line of reasoning above, and change by roughly 25% between $R = 1$ nm and $R \to \infty$ for F-SAMs. The extrapolated values at $R^{-2} = 0$ are in good agreement with LJ PME MD simulation results for both SAM types, also shown.

In real systems, SAMs sit atop a solid gold surface, while in our simulations, SAMs are held in place by restraint potentials with only vacuum below. In the SI Section S5, the expected reduction in the extrapolated contact angles due to additional water-gold dispersion interactions is estimated, and found to be roughly 2.2° for H-SAMs and 2.1° for F-SAMs. This picture accords well with experimental data where increasing the length of SAM chain molecules, and thus increasing the water-gold distance, results in marginally more hydrophobic surfaces, e.g. $\theta_a = 111°$ for H11 vs. 115° for H22 [43], $\theta_a = 111°$ for H11 vs. 112° for H22 [44], and $\theta_a = 116°$ for H2F10 vs. 122° for H11F10 [45] (it is shown in the SI Section S5 that H-SAMs and F-SAMs are only roughly 22% as attractive to water as an equal volume of solid gold). The gold-adjusted extrapolated contact angles are also shown in Figure 3d as solid horizontal lines, and agree very well with experimental advancing contact angles for the same systems (H10 and H2F8) from Ref. [39], also shown. It should be noted that contact angles from equilibrium droplet simulations are more akin to static contact angles, which are intermediate between smaller receding and larger advancing contact angles, so the comparison should be consid-

6

ered with care. This is one reason we consider the difference $\theta_F - \theta_H$ below.

The R^{-2} dependence of interfacial properties in eq (12) and eq (13) vs. the R^{-3} dependence of bulk properties in eq (8) and eq (11) brings into sharp focus the limitation of finite force cutoffs in interfacial simulations. At interfaces, short cutoffs will have a much greater impact. This is exemplified by the fact that the dispersive potential energy and density of bulk water change only negligably between $R = 1$ nm and $R \to \infty$ whereas the wetting coefficient and dispersive SAM-water interaction energy both change significantly. This is a strong argument for trusting simulations with longer cutoffs for calculating interfacial properties, even when the force fields used were originally optimized for bulk properties using shorter cutoffs.

We also carried out experimental measurements of water contact angles for H-SAMs and F-SAMs. Figure 3e shows example photos of droplets on H-SAMs and F-SAMs used for goniometric measurements. Further experimental details are given in the Methods Section and in the SI Section S6. Figure 3f shows the difference $\theta_F - \theta_H$ from our experimental measurements and those from Ref. [39] (both of which are for exactly the same chemical compounds as used in the simulations), and from the extrapolated and LJ PME results shown in Figure 3d. This highlights how fluorination of decane SAMs consistently causes a roughly 5° increase in water contact angles.

SAM Number Density

At first blush, the increased hydrophobicity of F-SAMs might seem counterintuitive; the C–F bond is strongly dipolar with a negatively charged fluorine, so one might expect it to act as a hydrogen-bond acceptor. However, this tends not to be the case [14, 46]. There are several key differences in the structure of F-SAMs and H-SAMs: perfluorinated alkanes (F-chains) have weaker mutual interactions than their aliphatic counterparts (H-chains) [47], F-chains are fatter and stiffer and are helical, while H-chains tend to form a planar zig-zag structure [48]. These factors conspire to cause F-chains to pack less densely on the substrate than H-chains [48, 49].

Regarding both F-SAMs and H-SAMs on a Au(111) substrate, which consists of hexagonal close-packed atoms with a nearest-neighbor interatomic distance of 2.884 Å, there has been considerable disagreement regarding the superstructure of the sulfur ligand adlayer. For H-SAMs, proposed superstructures include incommensurate c(7 × 7) [50], commensurate $(\sqrt{3} \times \sqrt{3})$ R30° [39, 51], and more recently a c(4 × 2) structure involving vacancies and adatoms [52, 53]. For F-SAMs, they include both commensurate and incommensurate (2 × 2) [39, 51, 54, 55], and c(7 × 7) [55, 56], with general agreement that there is a 30° rotation of the superstructure with respect to the substrate. Fortunately, these disagreements regarding the ligand adlayer superstructure do not extend to the gross structure of the SAMs themselves. F-SAMs and H-SAMs on Au(111) have both been shown by AFM, grazing incidence X-ray diffraction, electron diffraction, and computational studies to comprise hexagonal close-packed structures, with typically cited grafting distances of $d_H = 4.97$ Å for H-SAMs and $d_F = 5.9$ Å for F-SAMs [39, 50, 51, 54, 56, 57]. As mentioned above, these are the values we take as defaults in our simulations. Figure 4a shows a snapshot of the bottom of a simulated F-SAM; instead of simulating a gold surface with a sulfur ligand adlayer, we restrain the bottom carbon atoms of the SAM adsorbate molecules in a close-packed lattice with grafting distance d, as indicated in the figure.

Because $d_F > d_H$, F-SAMs form a less densely packed ligand adlayer on the Au(111) substrate than do H-SAMs. Other factors held equal, a less-dense ligand adlayer implies a less-dense SAM, and lower density is regarded as the cause of the increased hydrophobicity of F-SAMs [49]. This is because dispersion interactions dominate the SAM-water interaction energy, and the lower number density of atoms in the F-SAM means weaker dispersion interactions with the solid near the interface [15, 49]. Indeed, experimental and theoretical studies have shown the dispersive work of adhesion to decrease significantly with increasing fluorination [15, 58].

It bears mentioning at this point why we restrict the discussion to dispersion interactions, and ignore the electrostatic contribution to the SAM-water interaction energy. For partially-fluorinated aliphatic SAMs comprising molecules of the form $SH(CH_2)_n(CF_2)_mCF_3$, there has been shown to be a significant dipole at the hydrocarbon-fluorocarbon bond, which can play a significant role when near the SAM surface [14, 15, 59, 60, 61]. In the most extreme case of an aliphatic molecule with a single fluorinated carbon $SH(CH_2)_nCF_3$, the electrostatic SAM-water interaction energy is experimentally estimated to make up roughly 30% of

the total [14, 15], and the surface shows a three-fold increase in friction over the aliphatic case [59]. However, as the length of fluorinated tails increases, the CH_2–CF_2 dipole is buried below the SAM surface, and for fluorinated tails longer than 4 or 5 carbons, the electrostatic energy becomes negligible and contact angles show little to no discernable change [14, 15]. Here, we restrict ourselves to H-SAMs, and F-SAMs with 8 fluorinated carbons at the tail, so a theoretical treatment limited to dispersion interactions is not unreasonable.

In agreement with Ref. [49], we find the larger ligand adlayer spacing for F-SAMs to be a primary cause of increased F-SAM hydrophobicity, but with the added caveat that the tilt angle also plays an important role. Figure 4b shows profiles along z of number densities of selected atoms and areal dispersive SAM-water interaction energy profiles from simulations of water slabs on H-SAMs and F-SAMs. Because $d_F > d_H$, the bulk number density of carbons is greater for the H-SAM, and it is greater for H atoms in the H-SAM than for F atoms in the F-SAM. The dispersive SAM-water interaction energy profiles in the lower panels of Figure 4b are constructed by binning all pairwise dispersive SAM-water interaction contributions according to the z-position and type of the SAM atom involved. This is done over 200 frames evenly spaced out over equilibrium trajectories. The fluorine contribution in the F-SAM is similar to that of the hydrogen in the H-SAM; fluorine's stronger Lennard-Jones interaction strength (OPLS-AA values: $\varepsilon_{HO} = 0.283$ kJ/mol, $\varepsilon_{FO} = 0.419$ kJ/mol) makes up for the decreased number density of the fluorine atoms. The energy contribution from carbon-water interactions is significantly diminished for the F-SAM due to the lower density however, indicating that the surface should be more hydrophobic. One final takeaway from the energy profiles in Figure 4b is that the dispersive SAM-water interaction energy is dominated by the atoms in the surface that are within 5 Å of the Gibbs dividing surface of the water slabs. Thus, in the case of dispersion interactions cut off at 1 nm, the details of structure deep in the SAM (> 5 Å) are relatively unimportant, except insofar as they affect structure nearer the surface.

Unlike in an experiment, in MD simulations, we may freely vary the grafting distance to better understand its effect on SAM structure and hydrophobicity; we simulate H-SAMs at $d = 4.1, 4.4, 4.7, 4.97, 5.3, 5.6,$ and 5.9 Å, and F-SAMs at $d = 5.0, 5.3, 5.6, 5.9, 6.2, 6.5,$ and 6.8 Å.

The main results are shown in Figures 4e-h. Figure 4e shows the contact angle from droplet extrapolation, θ. Contact angles increase significantly with increasing d for SAMs with smaller than preferred grafting distance. However, θ for both H-SAMs and F-SAMs shows less regular behavior beginning at that SAM's preferred grafting distance. For the H-SAMs, the trend even reverses, with θ decreasing between $d = 4.97$ and 5.3 Å, and the d dependence is rather weak for larger d. The F-SAMs show a similar, albeit less pronounced anomaly around 5.9 Å, with yet weaker dependence for larger d. This anomalous behavior can be explained in terms of tilt angle and its effect on SAM density.

Tilt Angle

Even for SAMs on atomistically flat substrates and free of defects, surface adlayer grafting distance is not the only factor influencing the number density of atoms in SAMs. Adsorbate molecules may tilt away from the surface normal, often in a coordinated manner, increasing SAM atomic number density. For H-SAMs on Au(111), simulation studies indicate a tilt angle ϕ of roughly 30° [62, 63, 64], while grazing X-ray diffraction indicates between 32-34° for decane SAMs on Au(111), with tilt lessening to about 30° for SAMs of longer H-chains [65]. For F-SAMs on Au(111), grazing incidence X-ray diffraction indicates a tilt angle of $12 \pm 2°$ [56], while infrared reflection-absorption spectroscopy (IRRAS) indicates 15-16° [39]. We also measure the tilt angle of an F-SAM on a gold film using surface-enhanced infrared absorption spectroscopy (SEIRAS), finding $\phi_F^{exp} = 16 \pm 4°$, in close agreement with the IRRAS result of Ref. [39], as detailed in the Methods Section and in the SI Section S7. The density of a SAM with a fixed adlayer grafting distance d should be proportional to $(\cos \phi)^{-1}$, which would imply, for example, that an increase in tilt angle from 0° to 34° should correspond to a 20% increase in SAM density. Therefore, given that hydrophobicity depends on bulk number density of atoms in the surface, the tilt angle should also play an important if indirect role.

Figure 4c shows snapshots of H-SAMs and F-SAMs, where the collective tilt is readily apparent. This tilt is easily measured from MD simulation data. Because our molecules of choice have an even number of carbons and a zig-zag structure, we do *not* take the molecular axis as that passing through the top and bottom carbons. Instead, the angles ϕ_1 and ϕ_2 are found between the surface normal and
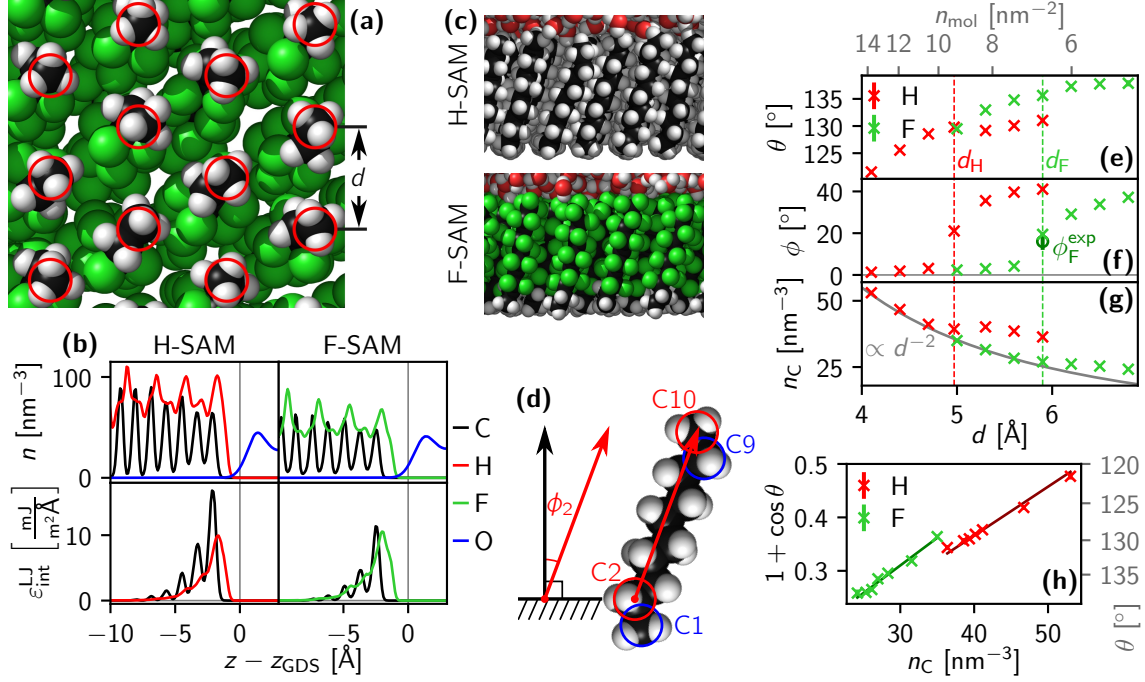
Figure 4: **(a)** A snapshot showing the bottom of a simulated F-SAM (H2F8). The bottom carbons are restrained by stiff harmonic potentials in a planar close-packed lattice with nearest-neighbor grafting distance d. These restraint positions are indicated by the red circles. **(b)** Profiles of atomic number densities for C, H (SAM only), F, and O atoms, for H-SAMs (H10) and F-SAMs (H2F8) under water slabs (top row); and dispersive SAM-water interaction energy profiles (bottom row). Here, pairwise dispersive SAM-water interactions are summed over and binned according to the z-position and type of the respective SAM atom. A positive contribution indicates an attractive force. **(c)** Simulation snapshots of an H-SAM and an F-SAM where the molecular tilt is apparant. **(d)** Schematic illustrating how the tilt angle is calculated from MD simulation data. Angles ϕ_1 and ϕ_2 are calculated between the surface normal and displacement vectors between carbons C1 and C9, and C2 and C10 respectively, and the tilt angle for that molecule is taken as their mean. **(e-g)** Droplet-extrapolation contact angle θ, mean tilt angle ϕ, and bulk number density of C atoms in the SAM n_C, for H-SAMs and F-SAMs, each plotted over the enforced SAM grafting distance d. The areal number density of SAM molecules n_{mol} is also shown on the upper axis. The experimental (SEIRAS) tilt angle for the F-SAM, ϕ_F^{exp}, is shown in (f) at the default F-SAM grafting distance $d = 5.90$ Å. **(h)** Contact angle data from droplet-extrapolation method, plotted in the form $1 + \cos\theta$ over the bulk number density of carbon atoms n_C in the SAM, shown with single-parameter linear fits of eq (18).

the displacement vectors between carbons C1 and C9, and C2 and C10 respectively, as illustrated in Figure 4d. The tilt angle for that molecule is then taken as their mean, and the mean of these is taken over the SAM and trajectory to give ϕ

Figure 4f plots the average tilt angle ϕ of H-SAMs and F-SAMs as a function of grafting distance d. For values of d below the respective preferred value d_H or d_F, tilt angles are less than 5°, with only weak d-dependence. Here, the SAMs are tightly packed, with molecules essentially restricted to the vertical. At and above the preferred values of d, molecules tilt to maintain energetically optimal distances between H or F atoms of nearest-neighbor molecules.

For the F-SAM with grafting distance d_F, we find a tilt angle of $\phi = 18.9 \pm 0.6°$, which compares rather well to our aforementioned experimental (SEIRAS) result of $\phi_F^{exp} = 16 \pm 4°$, also shown in the plot. For large grafting distances, ϕ approaches $\approx 40°$ for both H-SAMs and F-SAMs. Thus while increasing d reduces bulk SAM density, for large enough d, SAMs begin to tilt, which has the opposite effect, increasing the bulk density of the SAM. Indeed, Figure 4g shows the bulk number density of carbon atoms n_C extracted from water slab simulations, and it deviates noticably from the d^{-2} scaling behavior expected for the ligand adlayer grafting density (also plotted for reference) in tandem with the increase in tilt angle.

9

SAM Number Density Equation

The interplay between grafting distance and tilt angle can be subsumed into a more general discussion centered on the bulk number density of atoms in the surface. The work W of removing an adsorbed droplet from a solid surface can be written

$$W = A_{sl}(\gamma_{lv} - \gamma_{sl} + \gamma_{sv}), \qquad (14)$$

where γ_{lv}, γ_{sl}, and γ_{sv} are the surface tensions of the liquid-vapor, solid-liquid, and solid-vapor interfaces respectively, and A_{sl} is the area of the solid-liquid interface. Young's equation, derived in the SI Section S1, relates these surface tensions to the contact angle,

$$\cos\theta = \frac{\gamma_{sv} - \gamma_{sl}}{\gamma_{lv}}. \qquad (15)$$

Combining eq (14) and eq (15) gives

$$\gamma_{lv}(1 + \cos\theta) = \frac{W}{A_{sl}}. \qquad (16)$$

In the SI Section S4, it is shown that W scales like the SAM-water interaction energy ε_{int} for varying d. Further, in the approximation of the SAM as a homogeneous continuum, which includes the assumption that number densities n of different species of atoms in the SAM are proportional to one another (e.g. $n_{\text{H}} \approx 2n_{\text{C}}$ for an H-SAM), the SAM-water interaction energy should be proportional to the density of the solid, which should in turn be proportional to the number density of any atom, thus

$$W \propto \varepsilon_{\text{int}} \propto n_{\text{C}}. \qquad (17)$$

Combining eq (16) and eq (17) gives

$$1 + \cos\theta = \alpha\, n_{\text{C}}, \qquad (18)$$

where α is the (constant) slope depending on water density and the potential governing pairwise interactions between SAM and water. Eq (18) is also derived in more detail in the SI Section S8. Figure 4h shows droplet-extrapolation contact angle data plotted in the form $1 + \cos\theta$ over bulk number density of carbon atoms n_{C}, along with *single-parameter* least squares fits of eq (18). It should be stressed here that only α is adjusted and the fitted lines pass through the origin. The relationship holds remarkably well, and provides a means to clearly understand how SAM grafting distance and tilt angles influence hydrophobicity.

Roughness

Another structural characterisic of surfaces long known to be implicated in hydrophobicity is the surface roughness, the prototypical example of which is the lotus leaf. Indeed, many examples of nano- and/or microrough superhydrophobic surfaces can be found in nature [66]. Surfaces can be made rough on a nanoscopic scale by chemical etching, which for hydrophobic surfaces further increases their hydrophobicity [67]. Use cases include, for example, the reduction of biofouling in marine contexts, and the enhancement of osteoblast adhesion and growth on surfaces [67, 68]. Both decanethiol SAM surfaces and fluorinated surfaces have been shown to become more hydrophobic upon nanoroughening [69, 70].

Typically, the dependence of contact angle on surface roughness is described by the Wenzel and/or Cassie-Baxter equations [71, 72]. The Wenzel equation assumes a *Wenzel state*, where the liquid beneath the droplet penetrates fully among the roughness features, which increases the solid-liquid interfacial area, while the Cassie-Baxter equation assumes a *Cassie-Baxter state*, where the droplet is suspended at the upper extent of the roughness features, which decreases the solid-liquid interfacial area. However, both of these equations are formulated under the assumption of roughness consisting of features much larger than the distances over which intermolecular interactions are significant. Indeed, both the Wenzel and Cassie-Baxter equations have been shown to break down for roughness consisting of features smaller than about $10\times$ the diameter of the liquid molecules [73, 74]. In this work, the roughness studied is on a molecular scale, so the Wenzel and Cassie-Baxter *equations* are not used, but the penetration of the liquid into roughened surfaces is compared to Wenzel and Cassie-Baxter *states*.

We vary the roughness of SAMs in two primary ways. Recall that the SAMs are fixed in position via a harmonic potential applied to the bottom carbon of each molecule. Call the z-position of the potential minimum z_r. The first strategy is to loosen the restraint potentials on the bottom carbon atoms of the SAM molecules, which allows for larger thermal fluctuations of individual molecules up and down along z, resulting in a rougher surface. This we refer to as *dynamic* roughness. The second strategy, which we refer to as *static* roughness, is to shift the restraint position z_r of sublattices of the SAM up and down by a fixed distance. The SAM is divided into three triangular sublattices, each consisting of one-third of the molecules, and their restraint postions are set at three different heights along z, separated by a fixed distance Δz_r, as illustrated in Figure 5a.
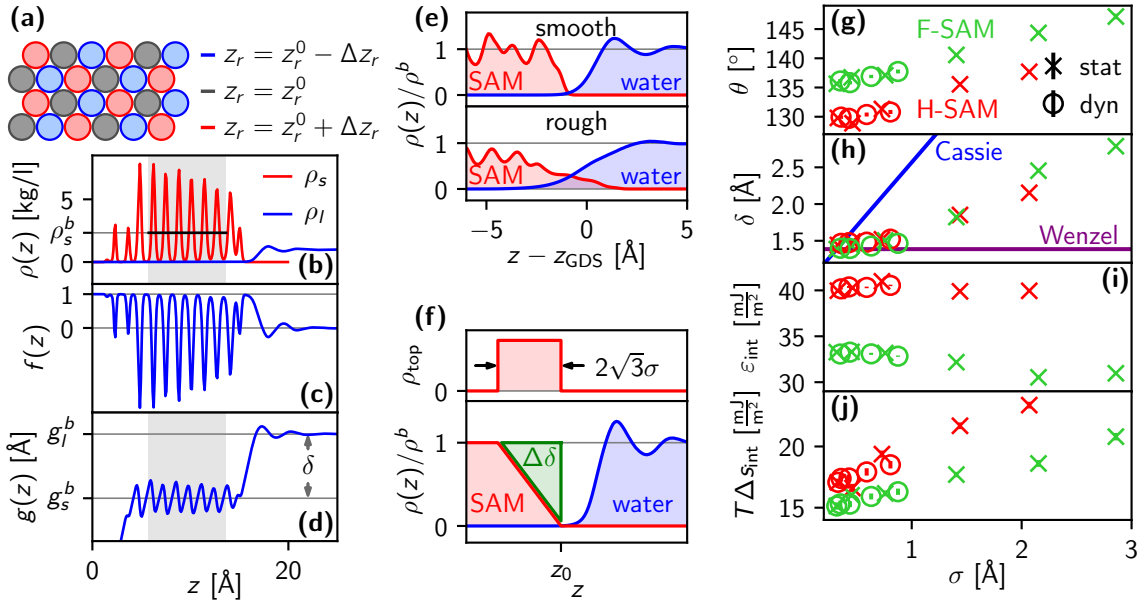
Figure 5: **(a)** Schematic illustrating sublattices for static roughness. The close-packed SAM, lying in the xy-plane, is split into three triangular sublattices as indicated by different colors in the figure, which are shifted to different heights along z. **(b-d)** Plots illustrating the method for determining the depletion length δ. **(b)** Mass density profiles of liquid and solid from a simulation of a water slab on an F-SAM. Also shown is the mean density of the solid in the bulk ρ_s^b, which is taken over the shaded region. **(c)** Density deficit $f(z)$ (eq (20)) obtained from the data in (b). **(d)** Cumulative integral $g(z)$ (eq (21)) of the density deficit in (c). Its mean value in the bulk of the SAM, g_s^b, is taken over the shaded region. Also shown is the depletion length δ. **(e)** Normalized mass density distributions of smooth ($\sigma = 0.32$ Å) and rough ($\sigma = 2.86$ Å) F-SAMs and water slabs. **(f)** Heuristic plot of the approximation used for the Cassie-Baxter scaling shown in (h). Tops of molecules are taken to be uniformly distributed over an interval of width $2\sqrt{3}\sigma$, as shown in the top panel, which gives a ramp-function distribution for the total SAM density, as shown in the bottom panel. The σ-dependent contribution to the depletion length is the area of the green triangle $\Delta\delta = \sqrt{3}\sigma$, as given by eq (22). **(g)** Water contact angles from droplet extrapolation for roughened H-SAMs (H10) and F-SAMs (H2F8), plotted over roughness. Roughness is engendered either by loosening the SAM restraint potential (dynamic) or shifting sublattices up and down along z by a fixed distance as in (a) (static). **(h)** Depletion length calculated according to eq (20), as illustrated in (b-d). Also shown is the scaling behavior for ideal Wenzel and Cassie-Baxter (as illustrated in (f)) states extrapolated from the smoothest F-SAM. **(i)** SAM-water interaction energy calculated by summing over pairwise interactions. **(j)** Adhesion entropy contribution to the work of adhesion calculated via eq (23).

For dynamic roughness, we carry out simulations with the spring constant in the z-direction set to $k_z = 25000$, 7500, 2500, 750, and 250 kJ/(mol nm^2). Restraint potentials looser than about 250 kJ/(mol nm^2) lead to significant deformation of the SAM by the adsorbed water droplet. For static roughness, we carry out simulations with sublattices shifted up and down by $\Delta z_r = 0.5$, 1, 2, 3, and 4 Å (though H-SAMs became unstable at $\Delta z_r = 4$ Å, so no contact angle data is given), with a stiff restraint potential of $k = 25000$ kJ/(mol nm^2). In either case, we characterize the roughness by the standard deviation among the z-positions of top carbons (C10), taking the time average of this quantity over an equilibrium trajectory

of a SAM under a water slab. Specifically, letting $z_i(t)$ be the z coordinate of the top carbon of the ith SAM molecule at time t, the roughness for a given SAM is characterized by

$$\sigma \equiv \langle\sigma_z(t)\rangle_t = \left\langle \sqrt{\langle z_i^2(t)\rangle_i - \langle z_i(t)\rangle_i^2} \right\rangle_t, \quad (19)$$

where $\langle\ldots\rangle_x$ denotes the arithmetic mean over x.

As mentioned above, Wenzel and Cassie-Baxter states describe the degree of penetration of the liquid into the roughened surface, an obvious metric for which is the density deficit at the interface. The zone of low density at a solid-liquid interface is called the depletion layer. The extent of depletion

11

in this layer may be quantified by the integral over the density deficit in this layer, called the depletion length,

$$\delta = \int_{z_s}^{z_l} \mathrm{d}z \, f(z) = \int_{z_s}^{z_l} \mathrm{d}z \left(1 - \frac{\rho_s(z)}{\rho_s^b} - \frac{\rho_l(z)}{\rho_l^b} \right), \tag{20}$$

where $\rho_s(z)$ and $\rho_l(z)$ are the solid and liquid density profiles, ρ_s^b and ρ_l^b are their respective bulk values, and z_s and z_l are z-positions well within the bulk of the solid and liquid respectively [35, 42, 75, 76, 77]. The integrand $f(z)$ is the density deficit and its cumulative integral we define as

$$g(z) = \int_{z_s}^{z} \mathrm{d}z' \, f(z') . \tag{21}$$

Figure 5b shows plots of mass densities of liquid and solid from a simulation of a water slab on an F-SAM. Figures 5c and d show the corresponding $f(z)$ and $g(z)$. The mean value for the SAM density ρ_s^b is taken over the shaded region in the plot. The region boundaries are chosen carefully so that the cumulative integral $g(z)$ has roughly net zero change in the solid. The depletion length δ may be calculated from the difference in the bulk values of $g(z)$ in the solid and liquid, as shown in Figure 5d.

Figure 5e shows density profiles of an F-SAM under a water slab for the smoothest ($\sigma = 0.32$ Å) and roughest ($\sigma = 2.86$ Å) F-SAMs simulated. There is little overlap between the water and the smooth SAM, but significant overlap between the water and the rough SAM, indicating that water penetrates somewhat into the roughened surface. For a Wenzel state, as the SAM roughens, water molecules should fill any spaces created, so the density deficit should remain unchanged. For a Cassie-Baxter state, the deficit depends on the SAM mass density profile along z and the position of the water slab. Figure 5f illustrates our chosen approximation. We take the tops of the SAM molecules to be uniformly distributed within a given interval along z. The width of the interval must be $2\sqrt{3}\sigma$, where σ is the standard deviation of the molecule tops. This gives a density distribution $\rho_s(z)$ for the SAM of a ramp function. Assuming there is no overlap between the water and SAM along z, and that the water slab is static relative to z_0 with changing σ, eq (20) gives

$$\delta_{\mathrm{CB}} = \sqrt{3}\sigma + \int_{z_0}^{z_l} \mathrm{d}z \left(1 - \frac{\rho_l(z)}{\rho_l^b} \right) = \sqrt{3}\sigma + C, \tag{22}$$

where C is constant in σ. Figure 5g shows contact angle data obtained via droplet extrapolation method for all simulated dynamic and static roughnesses, plotted over the roughness σ. It is apparant

that static and dynamic roughness both increase hydrophobicity, and by a very similar degree, for both H-SAMs and F-SAMs. Namely, the contact angle increases by about 5° per 1 Å increase in σ.

Figure 5h shows the depletion length as a function of roughness for H-SAMs and F-SAMs. The solid lines are the limiting cases of the Wenzel and Cassie-Baxter (slope of $\sqrt{3}\sigma$, see eq (22)) states extrapolated from the smoothest F-SAM. The measured depletion length increases monotonically, falling between these two limiting cases, with Wenzel-like behavior for low roughness, and increasingly Cassie-Baxter-like behavior for high roughness.

A higher degree of water penetration into the roughened surface should result in more conformational restriction of the water, and lower entropy in the adsorbed state. In the SI Section S4, it is shown that the work of adhesion may be written

$$W = A_{sl} \left(\varepsilon_{\mathrm{int}} - T \Delta s_{\mathrm{int}} \right), \tag{23}$$

where Δs_{int} is the areal adhesion entropy, i.e. the entropy change per unit area upon detachment due to SAM-water interactions [78]. Thus a lower entropy in the adsorbed state indicates a smaller work of adhesion and a more hydrophobic surface. Figure 5i shows $\varepsilon_{\mathrm{int}}$ from summing pairwise interactions in SAM-water slab simulations, and Figure 5j shows the adhesion entropy $T\Delta s_{\mathrm{int}}$, calculated via eq (23) using droplet extrapolation contact angles to obtain W, which is also detailed in the SI Section S4. It is clear that for both H-SAMs and F-SAMs, the entropic contributions $T\Delta s_{\mathrm{int}}$ change much more than the energetic contributions $\varepsilon_{\mathrm{int}}$ as roughness increases. Thus, unlike the cases of varying Lennard-Jones cutoff distance and SAM grafting distance, for which changes in hydrophobicity are shown to be due predominantly to changing SAM-water interaction energies (as shown in the SI Section S4 and evidenced by the linear behavior in Figures 3d and 4h), varying roughness affects hydrophobicity mainly via the entropy.

Conclusions

The increased hydrophobicity of F-SAMs over H-SAMs is primarily due to a reduced number density of atoms in the monolayer. Because perfluorination of alkanes has the effect of increasing their cross-sectional diameter, it tends to increase the nearest-neighbor grafting distance d and/or reduce the tilt angle ϕ in SAMs, thereby reducing their

bulk density, which leads to weaker interactions with adsorbed water, i.e. increased hydrophobicity. Specifically, it is found that the contact angle θ of a SAM is related to its bulk number density n via $1 + \cos\theta = \alpha n$, where α is a constant, characteristic of the type of molecules constituting the SAM.

Increasing the dispersion force cutoff distance R increases surface hydrophilicity, and extrapolation to the $R \to \infty$ limit gives contact angles that compare very favorably to those from LJ PME simulations and, when accounting for the gold substrate, to experimental values for both H-SAMs and F-SAMs. A comparison of the scaling behavior in the cutoff of bulk and interfacial properties provides strong evidence that for interfacial simulations, dispersion force cutoffs should be made as large as possible, regardless of the cutoff used in force field optimization.

Nanorough H-SAMs and F-SAMs are found to be more hydrophobic, with partial penetration of water into roughened surfaces, intermediate between Cassie-Baxter and Wenzel states. This increase in hydrophobicity for nanoroughened surfaces is found to be driven more by a decrease in adhesion entropy than an increase in SAM-water interaction energy.

References

[1] Butter, R.; Waterman, D.; Lettington, A.; Ramos, R.; Fordham, E. Production and wetting properties of fluorinated diamond-like carbon coatings. *Thin Solid Films* **1997**, *311*, 107–113.

[2] Ha, J.-W.; Park, I. J.; Lee, S.-B. Hydrophobicity and Sliding Behavior of Liquid Droplets on the Fluorinated Latex Films. *Macromolec.* **2005**, *38*, 736–744.

[3] Sundaram, H. S.; Cho, Y.; Dimitriou, M. D.; Finlay, J. A.; Cone, G.; Williams, S.; Handlin, D.; Gatto, J.; Callow, M. E.; Callow, J. A.; Kramer, E. J.; Ober, C. K. Fluorinated Amphiphilic Polymers and Their Blends for Fouling-Release Applications: The Benefits of a Triblock Copolymer Surface. *ACS Appl. Mater. Interfaces* **2011**, *3*, 3366–3374.

[4] Sanchez-Cano, C.; Carril, M. Recent Developments in the Design of Non-Biofouling Coatings for Nanoparticles and Surfaces. *Intl. J. Molec. Sci.* **2020**, *21*.

[5] Li, Q.; Yan, Y.; Yu, M.; Song, B.; Shi, S.; Gong, Y. Synthesis of polymeric fluorinated sol–gel precursor for fabrication of superhydrophobic coating. *Appl. Surf. Sci.* **2016**, *367*, 101–108.

[6] Li, S.; Huang, J.; Ge, M.; Li, S.; Xing, T.; Chen, G.; Liu, Y.; Zhang, K.; Al-Deyab, S.; Lai, Y. Controlled grafting superhydrophobic cellulose surface with environmentally-friendly short fluoroalkyl chains by ATRP. *Mater. Design* **2015**, *85*, 815–822.

[7] Yin, X.; Sun, C.; Zhang, B.; Song, Y.; Wang, N.; Zhu, L.; Zhu, B. A facile approach to fabricate superhydrophobic coatings on porous surfaces using cross-linkable fluorinated emulsions. *Chem. Eng. J.* **2017**, *330*, 202–212.

[8] Biffinger, J. C.; Kim, H. W.; DiMagno, S. G. The Polar Hydrophobicity of Fluorinated Compounds. *ChemBioChem* **2004**, *5*, 622–627.

[9] Schwierz, N.; Horinek, D.; Liese, S.; Pirzer, T.; Balzer, B. N.; Hugel, T.; Netz, R. R. On the Relationship between Peptide Adsorption Resistance and Surface Contact Angle: A Combined Experimental and Simulation Single-Molecule Study. *J. Amer. Chem. Soc.* **2012**, *134*, 19628–19638.

[10] Wertz, C. F.; Santore, M. M. Effect of Surface Hydrophobicity on Adsorption and Relaxation Kinetics of Albumin and Fibrinogen: Single-Species and Competitive Behavior. *Langmuir* **2001**, *17*, 3006–3016.

[11] Ulman, A. Formation and Structure of Self-Assembled Monolayers. *Chemical Reviews* **1996**, *96*, 1533–1554.

[12] Love, J. C.; Estroff, L. A.; Kriebel, J. K.; Nuzzo, R. G.; Whitesides, G. M. Self-Assembled Monolayers of Thiolates on Metals as a Form of Nanotechnology. *Chem. Rev.* **2005**, *105*, 1103–1170.

[13] Zenasni, O.; Jamison, A. C.; Lee, T. R. The impact of fluorination on the structure and properties of self-assembled monolayer films. *Soft Matter* **2013**, *9*, 6356–6370.

[14] Graupe, M.; Takenaga, M.; Koini, T.; Colorado, R.; Lee, T. R. Oriented Surface Dipoles Strongly Influence Interfacial Wettabilities. *J. Amer. Chem. Soc.* **1999**, *121*, 3222–3223.

[15] Colorado, R.; Lee, T. R. Wettabilities of Self-Assembled Monolayers on Gold Generated from Progressively Fluorinated Alkanethiols. *Langmuir* **2003**, *19*, 3288–3296.

[16] Wennberg, C. L.; Murtola, T.; Hess, B.; Lindahl, E. Lennard-Jones Lattice Summation in Bilayer Simulations Has Critical Effects on Surface Tension and Lipid Properties. *J. Chem. Theo. Comput.* **2013**, *9*, 3527–3537.

[17] Wennberg, C. L.; Murtola, T.; Páll, S.; Abraham, M. J.; Hess, B.; Lindahl, E. Direct-Space Corrections Enable Fast and Accurate Lorentz–Berthelot Combination Rule Lennard-Jones Lattice Summation. *J. Chem. Theo. Comput.* **2015**, *11*, 5737–5746.

[18] Berendsen, H.; van der Spoel, D.; van Drunen, R. GROMACS: A message-passing parallel molecular dynamics implementation. *Comp. Phys. Comm.* **1995**, *91*, 43–56.

[19] Lindahl, E.; Hess, B.; Van Der Spoel, D. GROMACS 3.0: a package for molecular simulation and trajectory analysis. *Molec. model. ann.* **2001**, *7*, 306–317.

[20] Hockney, R.; Goel, S.; Eastwood, J. Quiet high-resolution computer models of a plasma. *J. Comp. Phys.* **1974**, *14*, 148 – 158.

[21] Bussi, G.; Donadio, D.; Parrinello, M. Canonical sampling through velocity rescaling. *J. Chem. Phys.* **2007**, *126*, 014101.

[22] Jorgensen, W. L.; Madura, J. D.; Swenson, C. J. Optimized intermolecular potential functions for liquid hydrocarbons. *J. Amer. Chem. Soc.* **1984**, *106*, 6638–6646.

[23] Kaminski, G.; Duffy, E. M.; Matsui, T.; Jorgensen, W. L. Free Energies of Hydration and Pure Liquid Properties of Hydrocarbons from the OPLS All-Atom Model. *J. Phys. Chem.* **1994**, *98*, 13077–13082.

[24] Jorgensen, W. L.; Maxwell, D. S.; Tirado-Rives, J. Development and Testing of the OPLS All-Atom Force Field on Conformational Energetics and Properties of Organic Liquids. *J. Amer. Chem. Soc.* **1996**, *118*, 11225–11236.

[25] Berendsen, H. J. C.; Grigera, J. R.; Straatsma, T. P. The missing term in effective pair potentials. *J. Phys. Chem.* **1987**, *91*, 6269–6271.

[26] Watkins, E. K.; Jorgensen, W. L. Perfluoroalkanes: Conformational Analysis and Liquid-State Properties from ab Initio and Monte Carlo Calculations. *J. Phys. Chem. A* **2001**, *105*, 4118–4125.

[27] Hutter, J.; Iannuzzi, M.; Schiffmann, F.; VandeVondele, J. cp2k: atomistic simulations of condensed matter systems. *Wiley Interdisciplinary Reviews: Computational Molecular Science* **2014**, *4*, 15–25.

[28] Becke, A. D. Density-functional exchange-energy approximation with correct asymptotic behavior. *Phys. Rev. A* **1988**, *38*, 3098–3100.

[29] Grimme, S.; Antony, J.; Ehrlich, S.; Krieg, H. A consistent and accurate ab initio parametrization of density functional dispersion correction (DFT-D) for the 94 elements H-Pu. *J. Chem. Phys.* **2010**, *132*, 154104.

[30] Goedecker, S.; Teter, M.; Hutter, J. Separable dual-space Gaussian pseudopotentials. *Phys. Rev. B* **1996**, *54*, 1703–1710.

[31] Gillan, M. J.; Alfè, D.; Michaelides, A. Perspective: How good is DFT for water? *J. Chem. Phys.* **2016**, *144*, 130901.

[32] Korhonen, J. T.; Huhtamäki, T.; Ikkala, O.; Ras, R. H. A. Reliable Measurement of the Receding Contact Angle. *Langmuir* **2013**, *29*, 3858–3863.

[33] de Ruijter, M. J.; Blake, T. D.; De Coninck, J. Dynamic Wetting Studied by Molecular Modeling Simulations of Droplet Spreading. *Langmuir* **1999**, *15*, 7836–7847.

[34] Kanduč, M.; Eixeres, L.; Liese, S.; Netz, R. R. Generalized line tension of water nanodroplets. *Phys. Rev. E* **2018**, *98*, 032804.

[35] Sedlmeier, F.; Janecek, J.; Sendner, C.; Bocquet, L.; Netz, R. R.; Horinek, D. Water at polar and nonpolar solid walls (Review). *Biointerphases* **2008**, *3*, FC23–FC39.

[36] Kanduč, M. Going beyond the standard line tension: Size-dependent contact angles of water nanodroplets. *J. Chem. Phys.* **2017**, *147*, 174701.

[37] Bonthuis, D. J.; Gekle, S.; Netz, R. R. Profile of the Static Permittivity Tensor of Water at Interfaces: Consequences for Capacitance, Hydration Interaction and Ion Adsorption. *Langmuir* **2012**, *28*, 7679–7694.

14

[38] Gaydos, J.; Neumann, A. The dependence of contact angles on drop size and line tension. *J. Colloid Interface Sci.* **1987**, *120*, 76–86.

[39] Chidsey, C. E. D.; Loiacono, D. N. Chemical functionality in self-assembled monolayers: structural and electrochemical properties. *Langmuir* **1990**, *6*, 682–691.

[40] Ismail, A. E.; Grest, G. S.; Stevens, M. J. Capillary waves at the liquid-vapor interface and the surface tension of water. *J. Chem. Phys.* **2006**, *125*, 014702.

[41] in 't Veld, P. J.; Ismail, A. E.; Grest, G. S. Application of Ewald summations to long-range dispersion forces. *J. Chem. Phys.* **2007**, *127*, 144711.

[42] Sendner, C.; Horinek, D.; Bocquet, L.; Netz, R. R. Interfacial Water at Hydrophobic and Hydrophilic Surfaces: Slip, Viscosity, and Diffusion. *Langmuir* **2009**, *25*, 10768–10781.

[43] Folkers, J. P.; Laibinis, P. E.; Whitesides, G. M. Self-assembled monolayers of alkanethiols on gold: the adsorption and wetting properties of monolayers derived from two components with alkane chains of different lengths. *J. Adhesion Sci. Tech.* **1992**, *6*, 1397–1410.

[44] Bain, C. D.; Whitesides, G. M. Formation of monolayers by the coadsorption of thiols on gold: variation in the length of the alkyl chain. *J. Amer. Chem. Soc.* **1989**, *111*, 7164–7175.

[45] Fukushima, H.; Seki, S.; Nishikawa, T.; Takiguchi, H.; Tamada, K.; Abe, K.; Colorado, R.; Graupe, M.; Shmakova, O. E.; Lee, T. R. Microstructure, Wettability, and Thermal Stability of Semifluorinated Self-Assembled Monolayers (SAMs) on Gold. *J. Phys. Chem. B* **2000**, *104*, 7417–7423.

[46] O'Hagan, D. Understanding organofluorine chemistry. An introduction to the C–F bond. *Chem. Soc. Rev.* **2008**, *37*, 308–319.

[47] Mukerjee, P.; Handa, T. Adsorption of fluorocarbon and hydrocarbon surfactants to air-water, hexane-water and perfluorohexane-water interfaces. Relative affinities and fluorocarbon-hydrocarbon nonideality effects. *J. Phys. Chem.* **1981**, *85*, 2298–2303.

[48] Krafft, M. P.; Goldmann, M. Monolayers made from fluorinated amphiphiles. *Curr. Opin. Colloid Interface Sci.* **2003**, *8*, 243–250.

[49] Dalvi, V. H.; Rossky, P. J. Molecular origins of fluorocarbon hydrophobicity. *Proc. Nat. Acad. Sci.* **2010**, *107*, 13603–13607.

[50] Strong, L.; Whitesides, G. M. Structures of self-assembled monolayer films of organosulfur compounds adsorbed on gold single crystals: electron diffraction studies. *Langmuir* **1988**, *4*, 546–558.

[51] Alves, C. A.; Porter, M. D. Atomic force microscopic characterization of a fluorinated alkanethiolate monolayer at gold and correlations to electrochemical and infrared reflection spectroscopic structural descriptions. *Langmuir* **1993**, *9*, 3507–3512.

[52] Liu, Y.; Ozolins, V. Self-Assembled Monolayers on Au(111): Structure, Energetics, and Mechanism of Reconstruction Lifting. *J. Phys. Chem. C* **2012**, *116*, 4738–4747.

[53] Cossaro, A.; Mazzarello, R.; Rousseau, R.; Casalis, L.; Verdini, A.; Kohlmeyer, A.; Floreano, L.; Scandolo, S.; Morgante, A.; Klein, M. L.; Scoles, G. X-ray Diffraction and Computation Yield the Structure of Alkanethiols on Gold(111). *Science* **2008**, *321*, 943–946.

[54] Jaschke, M.; Schönherr, H.; Wolf, H.; Butt, H.-J.; Bamberg, E.; Besocke, M. K.; Ringsdorf, H. Structure of Alkyl and Perfluoroalkyl Disulfide and Azobenzenethiol Monolayers on Gold(111) Revealed by Atomic Force Microscopy. *J. Phys. Chem.* **1996**, *100*, 2290–2301.

[55] Barriet, D.; Lee, T. Fluorinated self-assembled monolayers: composition, structure and interfacial properties. *Curr. Opin. Colloid Interface Sci.* **2003**, *8*, 236–242.

[56] Liu, G.; Fenter, P.; Chidsey, C. E. D.; Ogletree, D. F.; Eisenberger, P.; Salmeron, M. An unexpected packing of fluorinated n-alkane thiols on Au(111): A combined atomic force microscopy and x-ray diffraction study. *J. Chem. Phys.* **1994**, *101*, 4301–4306.

[57] Ulman, A.; Eilers, J. E.; Tillman, N. Packing and molecular orientation of alkanethiol monolayers on gold surfaces. *Langmuir* **1989**, *5*, 1147–1152.

[58] Takenaga, M.; Jo, S.; Graupe, M.; Lee, T. R. Effective van der Waals surface energy of self-assembled monolayer films having systematically varying degrees of molecular fluorination. *J. Colloid Interface Sci.* **2008**, *320*, 264–267.

[59] Kim, H. I.; Koini, T.; Lee, T. R.; Perry, S. S. Systematic Studies of the Frictional Properties of Fluorinated Monolayers with Atomic Force Microscopy: Comparison of CF3- and CH3-Terminated Films. *Langmuir* **1997**, *13*, 7192–7196.

[60] Alloway, D. M.; Hofmann, M.; Smith, D. L.; Gruhn, N. E.; Graham, A. L.; Colorado, R.; Wysocki, V. H.; Lee, T. R.; Lee, P. A.; Armstrong, N. R. Interface Dipoles Arising from Self-Assembled Monolayers on Gold: UV–Photoemission Studies of Alkanethiols and Partially Fluorinated Alkanethiols. *J. Phys. Chem. B* **2003**, *107*, 11690–11699.

[61] Zenasni, O.; Marquez, M. D.; Jamison, A. C.; Lee, H. J.; Czader, A.; Lee, T. R. Inverted Surface Dipoles in Fluorinated Self-Assembled Monolayers. *Chem. Mater.* **2015**, *27*, 7433–7446.

[62] Hautman, J.; Klein, M. L. Simulation of a monolayer of alkyl thiol chains. *J. Chem. Phys.* **1989**, *91*, 4994–5001.

[63] Sellers, H.; Ulman, A.; Shnidman, Y.; Eilers, J. E. Structure and binding of alkanethiolates on gold and silver surfaces: implications for self-assembled monolayers. *J. Amer. Chem. Soc.* **1993**, *115*, 9389–9401.

[64] Mar, W.; Klein, M. L. Molecular dynamics study of the self-assembled monolayer composed of S(CH2)14CH3 molecules using an all-atoms model. *Langmuir* **1994**, *10*, 188–196.

[65] Fenter, P.; Eberhardt, A.; Liang, K. S.; Eisenberger, P. Epitaxy and chainlength dependent strain in self-assembled monolayers. *J. Chem. Phys.* **1997**, *106*, 1600–1608.

[66] Darmanin, T.; Guittard, F. Superhydrophobic and superoleophobic properties in nature. *Mater. Today* **2015**, *18*, 273–285.

[67] Zhang, H.; Lamb, R.; Lewis, J. Engineering nanoscale roughness on hydrophobic surface—preliminary assessment of fouling behaviour. *Sci. Tech. Adv. Mater.* **2005**, *6*, 236–239.

[68] Padial-Molina, M.; Galindo-Moreno, P.; Fernández-Barbero, J. E.; O'Valle, F.; Jódar-Reyes, A. B.; Ortega-Vinuesa, J. L.; Ramón-Torregrosa, P. J. Role of wettability and nanoroughness on interactions between osteoblast and modified silicon surfaces. *Acta Biomaterialia* **2011**, *7*, 771–778.

[69] Kijlstra, J.; Reihs, K.; Klamt, A. Roughness and topology of ultra-hydrophobic surfaces. *Coll. Surf. A* **2002**, *206*, 521–529.

[70] Mammen, L.; Deng, X.; Untch, M.; Vijayshankar, D.; Papadopoulos, P.; Berger, R.; Riccardi, E.; Leroy, F.; Vollmer, D. Effect of Nanoroughness on Highly Hydrophobic and Superhydrophobic Coatings. *Langmuir* **2012**, *28*, 15005–15014.

[71] Wenzel, R. N. Resistance of Solid Surfaces to Wetting by Water. *Ind. Eng. Chem.* **1936**, *28*, 988–994.

[72] Cassie, A. B. D.; Baxter, S. Wettability of porous surfaces. *Trans. Faraday Soc.* **1944**, *40*, 546–551.

[73] Grzelak, E. M.; Errington, J. R. Nanoscale Limit to the Applicability of Wenzel's Equation. *Langmuir* **2010**, *26*, 13297–13304.

[74] Kumar, V.; Errington, J. R. Impact of Small-Scale Geometric Roughness on Wetting Behavior. *Langmuir* **2013**, *29*, 11815–11820.

[75] Mamatkulov, S. I.; Khabibullaev, P. K.; Netz, R. R. Water at Hydrophobic Substrates: Curvature, Pressure, and Temperature Effects. *Langmuir* **2004**, *20*, 4756–4763.

[76] Maccarini, M.; Steitz, R.; Himmelhaus, M.; Fick, J.; Tatur, S.; Wolff, M.; Grunze, M.; Janeček, J.; Netz, R. R. Density Depletion at Solid–Liquid Interfaces: a Neutron Reflectivity Study. *Langmuir* **2007**, *23*, 598–608.

[77] Janeček, J.; Netz, R. R. Interfacial Water at Hydrophobic and Hydrophilic Surfaces: Depletion versus Adsorption. *Langmuir* **2007**, *23*, 8417–8429.

[78] Taherian, F.; Leroy, F.; van der Vegt, N. F. A. Interfacial Entropy of Water on Rigid Hydrophobic Surfaces. *Langmuir* **2013**, *29*, 9807–9813.